Research Article

Frequency-Dependent Streaming Potential of Porous Media—Part 2: Experimental Measurement of Unconsolidated Materials

P. W. J. Glover,[1] E. Walker,[1] J. Ruel,[2] and E. Tardif[2]

[1] *Department of Geology and Engineering Geology, Laval University, Québec City, QC, Canada G1K 7P4*
[2] *Department of Mechanical Engineering, Laval University, Québec City, QC, Canada G1K 7P4*

Correspondence should be addressed to P. W. J. Glover, paglover@ggl.ulaval.ca

Frequency-dependent streaming potential coefficient measurements have been made upon Ottawa sand and glass bead packs using a new apparatus that is based on an electromagnetic drive. The apparatus operates in the range 1 Hz to 1 kHz with samples of 25.4 mm diameter up to 150 mm long. The results have been analysed using theoretical models that are either (i) based upon vibrational mechanics, (ii) treat the geological material as a bundle of capillary tubes, or (iii) treat the material as a porous medium. The best fit was provided by the Pride model and its simplification, which is satisfying as this model was conceived for porous media rather than capillary tube bundles. Values for the transition frequency were derived from each of the models for each sample and were found to be in good agreement with those expected from the independently measured effective pore radius of each material. The fit to the Pride model for all four samples was also found to be consistent with the independently measured steady-state permeability, while the value of the streaming potential coefficient in the low-frequency limit was found to be in good agreement with other steady-state streaming potential coefficient data.

1. Introduction

There have only been 10 measurements of the frequency-dependent streaming potential coefficient of porous geological and engineering materials. A review of the existing measurements was carried out by Glover et al. [1]. These previous measurements can be divided into two groups: (i) transient measurements with a percussive source and (ii) harmonic measurements with a vibrating source.

While the first of these approaches mimics many of the possible applications more closely [2–4], it cannot provide the streaming potential coupling coefficient as a function of frequency without using the frequency domain filtering and Fourier techniques. Such techniques can only be used in a linear system. Although the equations that describe the streaming potential coefficient are linear below the transition frequency and there is no evidence that they become non-linear above that frequency, it has not yet been shown that such an approach can be made to work for streaming po-

tential coupling coefficient measurements on rocks. The processing of such data has, however, been discussed at length in Reppert and Morgan [5]; they mention that inertial effects may be seen if the transient signal has strong enough high-frequency components.

The second approach is capable of providing the streaming potential coupling coefficient at each frequency directly. Its disadvantage is that a high-quality harmonic driving pressure is required to create the time-varying flow. Various authors have shown that measurements on a range of materials are possible in the range 1 Hz to 600 Hz [6–10], but before the recent paper of Tardif et al. [11] only one measurement had been made on a geological material [10].

This paper reports research that uses the electromagnetic drive concept proposed by Glover et al. [1] to create an apparatus for measuring the frequency-dependent streaming potential coupling coefficient of unconsolidated materials such as sands, gravels, and soils. Unconsolidated materials were chosen because it is easier to arrange a sample holder

with no need for a sleeve and a sleeve pressure. The experimental data have been analyzed using a number of theoretical models. The first part of this paper is dedicated to describing these models, followed by experimental measurements on samples of sand and glass beads. The theoretical models have been compared with the measured data in order to obtain the transition frequency, which has then been used to calculate the effective pore radius of the sands and glass bead packs using the theory in Glover and Walker [12].

2. Theoretical Models

The steady-state streaming potential coefficient (the streaming potential per driving fluid pressure difference) has long been described by the Helmholtz-Smoluchowski (HS) equation, and is given in the form most convenient for application to rocks (e.g., [13]);

$$C_{so} = \frac{\Delta V}{\Delta P} = \frac{\varepsilon \zeta}{\eta_f \sigma}, \quad \text{where} \quad \sigma = \sigma_f + \frac{2\Sigma_s}{\Lambda}. \quad (1)$$

In this equation ΔP (Pa) is the fluid pressure difference, ε (F/m) is the dielectric constant of the fluid, η_f (Pa.s) is the dynamic viscosity of the fluid, ζ (V) is the zeta potential, ΔV (V) is the streaming potential, σ_f (S/m) is the electrical conductivity of the bulk fluid, Σ_s (S) is the specific electrical conductance of the surface (i.e., that due to the double layer), σ (S/m) is the electrical conductivity of the mobile fluid, and Λ (m) is a characteristic length associated with the microstructure of the pore network [14–18]. The steady-state streaming potential is independent of the sample geometry.

The importance of considering the surface conductance when applying the HS equation to geological materials has been discussed by a number of authors including [1, 14–17]. Recently several modified versions of the classical HS equation have been published that take into account the variability of the streaming potential coupling coefficient as a function of grain size [17, 19–21], pore size [17], and pore throat size [17].

There are several theoretical models for the frequency-dependent streaming potential coupling coefficient. The models fall into three categories: (i) models based only on vibrational mechanics [22], (ii) models based on flow in capillary bundles [6], and (iii) those that have been developed for porous media [23].

2.1. Vibrational Mechanics Models.
If we apply the amplitude of the critically damped second-order vibrational behaviour [22] to the frequency-dependent streaming potential coupling coefficient, we get

$$\frac{C_s(\omega)}{C_{so}} = \left(1 + \left(\frac{\omega}{\omega_t}\right)^2\right)^{-1/2}, \quad (2)$$

where $C_s(\omega)$ (in V/MPa) is the streaming potential coupling coefficient at a frequency ω (in Hz), C_{so} (in V/MPa) is the steady-state streaming potential coupling coefficient, and ω_t (in Hz) is the transition frequency. This model only exists in the real domain and is a special case (for $\xi = 1$) of the general

second-order vibrational behaviour with variable damping that is given by

$$\frac{C_s(\omega)}{C_{so}} = \left(\left(1 - \left(\frac{\omega}{\omega_t}\right)^2\right)^2 + \left(2\xi\left(\frac{\omega}{\omega_t}\right)\right)^2\right)^{-1/2}, \quad (3)$$

for the frequency-dependent streaming potential coupling coefficient. In this equation ξ is the damping factor of the system. This equation provides the modulus or magnitude of the vibration as is usually measured experimentally either by a peak-to-peak or an RMS measurement.

Both equations can be fitted to experimental data where $C_s(\omega)/C_{so}$ is plotted as a function of frequency. For (2) the transition frequency is the only fitting variable, while (3) has two fitting variables: the transition frequency and the damping factor.

These vibrational mechanics models are purely formal and contain no underlying physics. They are interesting in that they can show that a system is behaving in a certain manner, but no inference can be made, for example, about what controls the damping coefficient. This lack of specificity often allows such models to apparently fit the data better than other models which include more of the underlying physics.

2.2. Capillary Tube Models.
The capillary tube model was introduced by Packard [6] together with a small number of experimental measurements. It is given by

$$\frac{C_s(\omega)}{C_{so}} = \left(\frac{-2}{kr}\frac{J_1(kr)}{J_0(kr)}\right), \quad (4)$$

where

$$k^2 = \frac{-i\omega\rho_f}{\eta_f}, \quad (5)$$

where $i = \sqrt{-1}$, ρ_f (kg/m³) is the density of the bulk fluid, ω (rad/s) is the angular frequency, r (m) is the radius of the capillary in which the flow takes place, and J_0 and J_1 are Bessel functions of the zeroth and first order, respectively. Note that k has dimensions of inverse length; hence, kr is dimensionless, and the real part of the Bessel function expression $\Re[(2J_1(kr)/krJ_0(kr))]$ varies between unity at low frequencies and zero at high frequencies, and its imaginary part $\Im[(2J_1(kr)/krJ_0(kr))]$ is zero at both low and high frequencies, but attains a peak value at a frequency known as the transition frequency.

Reppert et al. [9] have provided a simplification of (4):

$$\frac{C_s(\omega)}{C_{so}} = \left(1 - \frac{2}{r}\sqrt{\frac{\eta_f}{\omega\rho_f}}\left\{\frac{1}{\sqrt{2}} - \frac{1}{\sqrt{2}}i\right\}\right), \quad (6)$$

(their Equations 26 and 38). However, a recent study showed that the simplification is incorrect [11]. The correct simplification, which is consistent with the simplified model solution shown in their Figure 4 [9] (T. Ishido, pers. comm., 2011), is

$$\frac{C_s(\omega)}{C_{so}} = \left(1 + \left[\frac{-2}{r}\sqrt{\frac{\eta_f}{\omega\rho_f}}\left\{\frac{1}{\sqrt{2}} - \frac{1}{\sqrt{2}}i\right\}\right]^{-2}\right)^{-1/2}. \quad (7)$$

When (4) or (7) is fitted to experimental data where the viscosity and density of the process fluid is known, the only fitting variable is the effective capillary radius r.

2.3. Porous Media Models.

An extremely important study by Pride [23] has provided a model of streaming potential coupling coefficient for porous media. It takes the form

$$
C_s(\omega) = \left(\frac{\varepsilon \zeta}{\eta_f \sigma} \left\{ 1 - 2\frac{\delta}{\Lambda} \right\} \right)
$$
$$
\times \left(1 - i\frac{\omega}{\omega_t}\frac{m^*}{4}\left\{ 1 - 2\frac{\delta}{\Lambda} \right\}^2\left\{ 1 - i^{3/2}\delta\sqrt{\frac{\omega\rho_f}{\eta_f}} \right\}^2 \right)^{-1/2},
\tag{8}
$$

where

$$
\omega_t \equiv \frac{\phi}{\tau_e \kappa_{DC}} \frac{\eta_f}{\rho_f},
\tag{9}
$$

and

$$
m^* \equiv \frac{\phi \Lambda^2}{\tau_e \kappa_{DC}}.
\tag{10}
$$

Equation (8) can be rewritten in the same form as the previous models as

$$
\frac{C_s(\omega)}{C_{so}} = \left(1 - i\frac{\omega}{\omega_t}\frac{m^*}{4}\left\{ 1 - 2\frac{\delta}{\Lambda} \right\}^2\left\{ 1 - i^{3/2}\delta\sqrt{\frac{\omega\rho_f}{\eta_f}} \right\}^2 \right)^{-1/2},
\tag{11}
$$

noting that the steady-state term in this model includes an additional factor $C_{so} = \varepsilon \zeta / (\eta_f \sigma) \{1 - 2(\delta/\Lambda)\}$.

In (8)–(11), τ_e (unitless) is the electrical tortuosity of the pore network, ϕ (unitless) is the porosity of the sample, κ_{DC} (m^2) is the steady-state fluid permeability, and δ (m) is the Debye length. The parameter ω_t (rad/s) is the transition frequency, at which the quadrature component of the dispersive system is greatest. While this equation may seem complex, it should be noted that for most geological media the pore fluid is sufficiently saline for the Debye length to be much smaller than the characteristic length scale (i.e., $\delta \ll \Lambda$), which allows significant simplifications to be made.

Recently, such a simplification of (11) has been proposed [19]:

$$
\frac{C_s(\omega)}{C_{so}} = \left(1 - i\frac{m^*}{4}\frac{\omega}{\omega_t} \right)^{-1/2},
\tag{12}
$$

where

$$
\omega_t = \frac{\phi}{\tau_e \kappa_{DC}}\frac{\eta_f}{\rho_f} = \frac{8}{r_{eff}^2}\frac{\eta_f}{\rho_f},
\tag{13}
$$

where r_{eff} (m) is the effective pore radius of the rock. Equation (12) makes the assumption that $\delta \ll \Lambda$, which is valid for the majority of porous rocks that are saturated with saline fluids with a concentration of 10^{-3} mol/dm^3 or more. If we take $m^* = 8/3$ as suggested by [19], we get

$$
\frac{C_s(\omega)}{C_{so}} = \left(1 - i\frac{2}{3}\frac{\omega}{\omega_t} \right)^{-1/2},
\tag{14}
$$

which is dependent solely on the transition frequency.

If either the full Pride model (11) or its simplifications (12) and (14) are fitted to experimental data where the viscosity and density of the pore fluid and the microstructural parameters ($\delta, \Lambda, \phi, \tau_e, \kappa_{DC}$) of the porous medium are known, the only fitting variable is the transition frequency.

2.4. Physical Interpretation of Theoretical Models.

Until recently only the Packard model [6] and its simplification [9] had been tested against data from a few measurements on capillary tubes and filter material [9, 10]. Recently [11] published some data for Ottawa sand which suggested that the vibrational mechanics models [22] fitted their data best. They reported that the best fit of all of the models was a damped second-order vibration mechanics model (3). However, there were errors in their data processing. A correct analysis of their data shows that their data follow the Pride model best, which agrees very well with the results of this study.

Most of the theoretical models have a real and imaginary part. In this paper we have analysed these two contributions separately, comparing the measured data with the overall magnitude and each of the complex components of each model. We have taken an RMS measurement approach which provides the magnitude of the variation and maximises the precision with which it can be measured.

It is interesting to consider the physical meaning of the real and imaginary contributions to the streaming potential coupling coefficient. Currently we do not have sufficient information to answer this question with authority. However, there are some indications. The streaming potential coupling coefficient is defined as the ratio of the streaming potential to the pressure drop across the sample. However, it is the fluid velocity that separates the charge and causes the streaming potential. This implies that the frequency dependence of the streaming potential coupling coefficient depends on the frequency dependence of the dynamic fluid permeability. The dynamic fluid permeability at low frequencies is controlled by viscous flow that is represented by the real part of the dynamic permeability. However, when a critical frequency is reached, the inertial acceleration of the fluid begins to control the flow (e.g., [9, 24]). The inertial acceleration is represented by the imaginary part of the dynamic permeability. Hence, we might expect the real and imaginary parts of the streaming potential coupling coefficient to be influenced by the same transition from viscous-dominated to inertial-dominated fluid flow. In this scenario, the transition frequency is the same as the critical frequency at which viscous-dominated fluid flow becomes inertially dominated. It is becoming clear, however, that the frequency dependence of fluid flow and of the streaming potential coupling coefficient are subtly different. The normalised

dynamic permeability of a bundle of capillary tubes approximately follows a Debye model for all frequencies, while the normalised streaming potential coupling coefficient follows the same Debye model up to the transition frequency then deviates from it considerably [25].

3. Experimental Tests

3.1. Sample Material and Basic Characteristics. Experimental tests were carried out on samples of Ottawa sand and on packs of glass beads using the apparatus described in the as- sociated paper [1]. Their main properties are shown in Table 1.

Ottawa Sand. Ottawa sand was obtained from Fisher Scientific and washed repeatedly in distilled water in order to remove any rock powder before being dried in a vacuum oven prior to use. The pore throat and grain size distributions of the sample material were measured using mercury injection porosimetry and are shown as Figure 1 in [11] together with the grain size distribution obtained by laser diffraction measurements using a Malvern Mastersizer 2000. The porosity of sand samples was also measured using a helium pycnometer. The complex electrical properties of a saturated sample of the sand were measured at 60 frequencies between 1 Hz and 1 MHz using a Solartron 1260A Impedance Analyzer. The absolute value of the complex electrical conductivity at the frequency for which the out-of-phase conductivity was minimum has been used together with the modal grain size from the laser diffraction measurements and the helium porosity in order to calculate the mean pore size of the sand samples using the method of [12].

The quasi-steady-state permeability was obtained by calculating the volume of fluid flowing through the sample per second at 10 Hz using the measured piston displacement and also measuring the pressure required to move this fluid. The permeability at 10 Hz was $\kappa_{10} = 1.19 \times 10^{-10}$ m^2. We have taken this value to represent the steady-state permeability in the absence of steady-state permeability on the sample.

The measurements shown in this paper are the same as those reported in [11]. However, it should be noted that there were major errors in the analysis of the data in [11] which are corrected in this work. Consequently, this work represents the correct treatment of the Ottawa sand data, while the previous paper should be referred to for a detailed petrophysical description of the material as well as measurements of the petrophysical properties of the Ottawa sand that have been made by other authors.

Glass Beads. Three sizes of soda lime glass bead (nominally 0.5, 1, and 2 mm in diameter) were obtained from Endecotts Ltd.. Samples of the beads were washed repeatedly in distilled water before being dried in a vacuum oven prior to use. No mercury porosimetry was carried out on the beads because they are too expensive to be disposed of after only one use. The grain size distribution was obtained by laser diffraction measurements and using the detailed calibration information provided by Endecotts Ltd., which is based on

a sieve analysis. The porosity of the glass bead samples was measured using a helium pycnometer. The complex electrical properties of a saturated sample of the sand were measured at 60 frequencies between 1 Hz and 1 MHz using a Solartron 1260A Impedance Analyzer, and the results were used to calculate the mean pore size of each bead pack using the Glover and Walker method [12] in the same way as for the Ottawa sand.

The steady-state permeability of each bead pack was measured using a gravitational pressure head. The results are shown in Table 1. These values are in very good agreement with the value predicted from the grain size and electrical measurements using the RGPZ method [26] (their Equation (10)).

Fluids. The fluid used in the experiments was 10^{-3} mol/L NaCl with a measured density of 997 kg/m^3, which agrees well with the equation of state of NaCl solutions (e.g., [27]) and a viscosity of 8.94×10^{-4} Pa.s calculated using the model of [28]. The electrical conductivity of the fluid was measured at $\sigma_f = [1.23 \pm 0.05] \times 10^{-2}$ S/m at 25°C before use, which is in good agreement with the model of Sen and Goode [29] at $[1.23 \pm 0.05] \times 10^{-2}$ S/m. For the Ottawa sand, the conductivity of the fluid emerging from the apparatus during the measurement was extremely close to the original conductivity of the fluid ($[1.21 \pm 0.05] \times 10^{-2}$ S/m at 25°C). In the case of the glass beads, the conductivity of the fluid slowly increased to 1.48×10^{-2} S/m, 1.38×10^{-2} S/m, and 1.33×10^{-2} S/m for 0.5, 1, and 2 mm diameter beads, respectively, while being circulated through the sample for 24 hours before the electrical and electrokinetic measurements were made. This amounts to an increase of concentration from 1×10^{-3} mol/L to 1.23×10^{-3} mol/L, 1.15×10^{-3} mol/L, and 1.10×10^{-3} mol/L, respectively, which we associate with dissolution of the grains during the attainment of physicochemical equilibrium between the grains and the fluid. For the Ottawa sand experiment, the pH of the fluid during the measurement was pH 6. In the case of the glass beads, the initial pH of the fluid was pH 6.9, which reduced during the recirculation of the fluids. The pH of the fluid was measured on samples of fluid emerging from the apparatus during the electrokinetic experiment. The stable values were pH 6.4, 6.6, and 6.7 for the 0.5, 1, and 2 mm diameter beads, respectively. We note again that the changes in the fluid conductivity and pH are not as great as some authors have experienced (e.g., Leroy et al. [30]), and we associate this with the repeated washings that we subjected the material to initially. However, we note later that modelling of the steady-state streaming potential coupling coefficient is extremely sensitive to the fluid conductivity and the pH. Hence it is extremely important for these parameters to be measured on the fluid emerging from the experimental apparatus during the electrokinetic measurement.

3.2. Experimental Methodology. The cell was loaded with either a sample of sand or beads in layers of 1 cm with light tamping between the layers in the case of the sand, and with agitation after each layer in the case of the glass beads.

TABLE 1: Physical properties of the sample material.

| Property	Unit	Ottawa sand	Glass beads			Comment
			0.5 mm	1 mm	2 mm	
Modal grain radius (laser diffraction), r_g	μm	251 ± 56	—	—	—	Using a Malvern Mastersizer 2000.
Modal grain radius (image analysis), r_g	μm	245 ± 46	249 ± 2.32	492 ± 11	995 ± 7	Image analysis using Sigma Scan 4.
Modal grain radius (Hg injection), r_g	μm	211 ± 59	—	—	—	Calculated from pressure data using Mayer-Stowe theory.
D10 grain radius (sieving), r_g	μm	—	251.1±0.200	493 ± 0.838	989.6±0.989	
Effective pore radius, r_p	μm	67.6 ± 16.2	70.8 ± 0.70	139 ± 3.41	287 ± 4.03	Using the method of Glover and Walker [12].
Effective pore throat radius, r_{pt}	μm	40.7 ± 9.0	42.7 ± 0.42	84 ± 2.06	173 ± 2.43	Using Glover and Déry [17], for random packing.
Modal pore throat radius (Hg injection), r_{pt}	μm	38.5 ± 7.5	—	—	—	Using a Micromeritics AutoPore IV
Porosity (gravimetry)	—	0.314	0.383	0.380	0.382	Please see text.
Porosity (helium expansion)	—	0.325	0.391	0.383	0.385	Using a real gas expansion pycnometer.
Porosity (mercury injection)	—	0.304	—	—	—	Using a Micromeritics AutoPore IV.
Measured permeability, κ_{meas}	m^2	1.19×10^{-10}	1.62×10^{-10}	5.95×10^{-10}	27.2×10^{-10}	The measured permeability at 5 Hz for the Ottawa sand and under steady-state conditions for the glass beads.
Predicted permeability using the RGPZ method, κ_{RGPZ}	m^2	1.22×10^{-10}	1.52×10^{-10}	5.80×10^{-10}	24.8×10^{-10}	Permeability predicted from electrical data and the grain diameter using the method of Glover et al. [26].
Electrical conductivity, σ_r	S/m	2.63×10^{-3}	3.58×10^{-3}	3.33×10^{-3}	3.32×10^{-3}	For a 0.001 mol/L NaCl at 25°C.
Electrical conductivity of the fluid, σ_f	S/m	1.23×10^{-2}	1.48×10^{-2}	1.38×10^{-2}	1.33×10^{-2}	Measured on the recycled fluid at the sample outlet after equilibration.
Formation factor, F	—	4.676	4.13	4.18	4.16	Calculated from the conductivities of the saturated rock and the saturating fluid.
Connectedness, G	—	0.214	0.242	0.239	0.241	Calculated from the formation factor [33, 34].
Cementation exponent, m	—	1.372	1.48	1.48	1.48	Calculated from the formation factor.
Electrical tortuosity, τ_e	—	1.519	1.583	1.589	1.588	Calculated from the porosity and m.
Theta factor, Θ	—	3.705	3.53	3.57	3.55	From the method of [12].
Predicted transition frequency, ω_t	Hz	256.48	213.36	57.32	12.61	At 24°C using the method of [19].
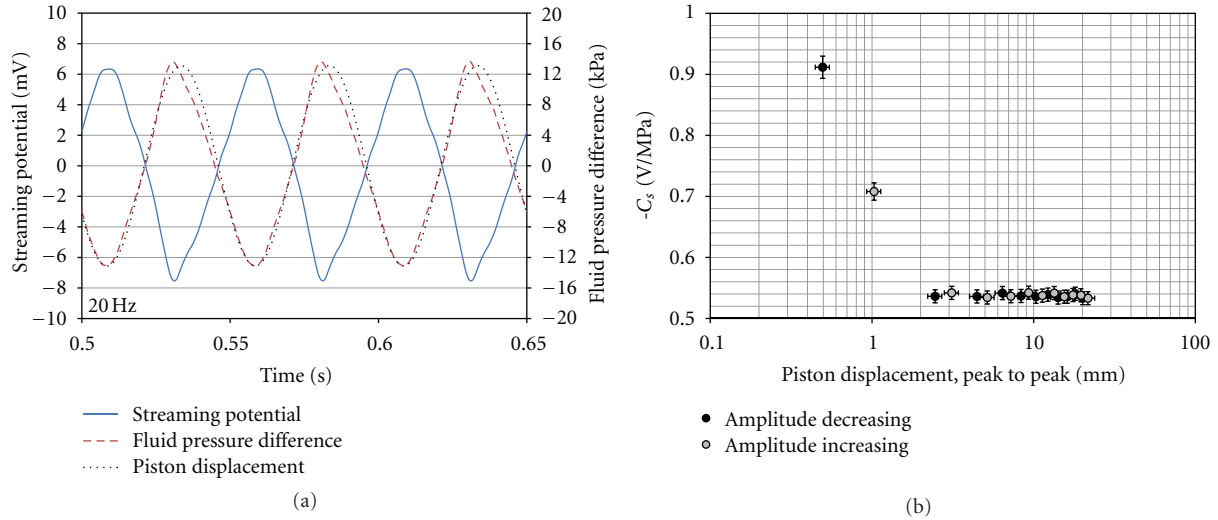
Figure 1: (a) The measured waveforms (streaming potential, fluid pressure and piston position (LVDT)) at 20 Hz. (b) The calculated streaming potential coupling coefficient as a function of piston amplitude at 10 Hz for Ottawa sand saturated with 10^{-3} mol/L NaCl solution at 24°C ($\phi = 0.325$, $\kappa_{10} = 1.19 \times 10^{-10}$ m^2). The errors in the frequency were calculated from the analysis of a train of approximately 500 cycles, while the errors in the streaming potential coupling coefficient were calculated from the errors in the RMS streaming potential and the measured RMS pressure difference (500 cycles).

The system was fully saturated with the process fluid, using back-pressure where necessary to remove all air bubbles. Once saturated, the steady-state permeability of the glass beads was measured using gravity-driven flow. The process fluid was then recycled through the sample for 24 hours to ensure full physicochemical equilibrium. During this time the permeability of the Ottawa sand was measured at a frequency of 10 Hz using the pressure transducers and calculating the flow by measuring the piston displacement with the LVDT.

Figure 1 shows the typical measured waveforms for 20 Hz, noting that there is a tendency that higher frequencies provide better-quality waveforms. High-quality measurements were possible between 5 and 200 Hz for the Ottawa sand and between 10 Hz and 500 Hz for the glass bead packs. Both the streaming potential and the dynamic pressure can be measured with acceptable levels of noise. Figure 1(a) shows that the fluid pressure and piston displacement are in phase with each other and in antiphase with the streaming potential, as theory requires. The compressive part of each cycle is sinusoidal as expected, whereas the backstroke is slightly distorted due to the inflow for new fluid through the check valve. This slight asymmetry might be corrected using digital filtering of the measured data or by imposing a background DC fluid flow and a back-pressure instead of using check valves. This latter approach would also remove any tendency for the fluid to cavitate.

In the case of Ottawa sand, tests were made up to 600 Hz, when the sample tube failed. It was observed that the seal between the piston and the tube let in air at frequencies higher than 200 Hz. Although the data for frequencies greater than 200 Hz seem to behave well, we have not reported them because the presence of air bubbles may make the measurements unreliable. We corrected the air leakage for the

glass bead pack measurements simply by lubricating the piston seal.

This paper contains results for three diameters of glass bead (0.5, 1, and 2 mm). We also attempted to make measurements on glass bead packs with a 0.25 mm and 3.35 mm nominal diameter. Unfortunately we could not generate sufficient pressure to produce a streaming potential of sufficient size to measure the 3.35 mm beads with accuracy, and the experiment with the 0.25 mm beads did not provide data of sufficient quality to report.

The frequency-dependent streaming potential coefficients were calculated using the methods described in Reppert et al. [9] and Reppert and Morgan [5], the most important step being the renormalisation of the data taking into account of the frequency-dependent impedance of the sample and measuring circuit, which is shown for each sample at each of the measurement frequencies in Figure 2. This procedure ensures that the streaming potential coefficient is calculated with the correct sample conductivity, that is, that which relates to the frequency of the data. Without such a step, the data seem to fit better the vibrational mechanics models, as was erroneously reported by us in [11]. Inclusion of the correction results in the data fitting the Pride model [23] better than the other models. This is a satisfying result as the Pride model was specifically conceived for porous media.

3.3. Displacement Tests. One of the characteristics of an electromagnetic shaker is that the piston amplitude decreases with frequency for any set driving current [1]. However, the differential fluid pressure generated by the piston increases with frequency [1]. If the driving current is kept constant throughout a suite of tests at different frequencies, the combination of these two effects is to generate smaller

(a) Ottawa sand

(b) Glass beads, $d = 0.5$ mm

(c) Glass beads, $d = 1$ mm
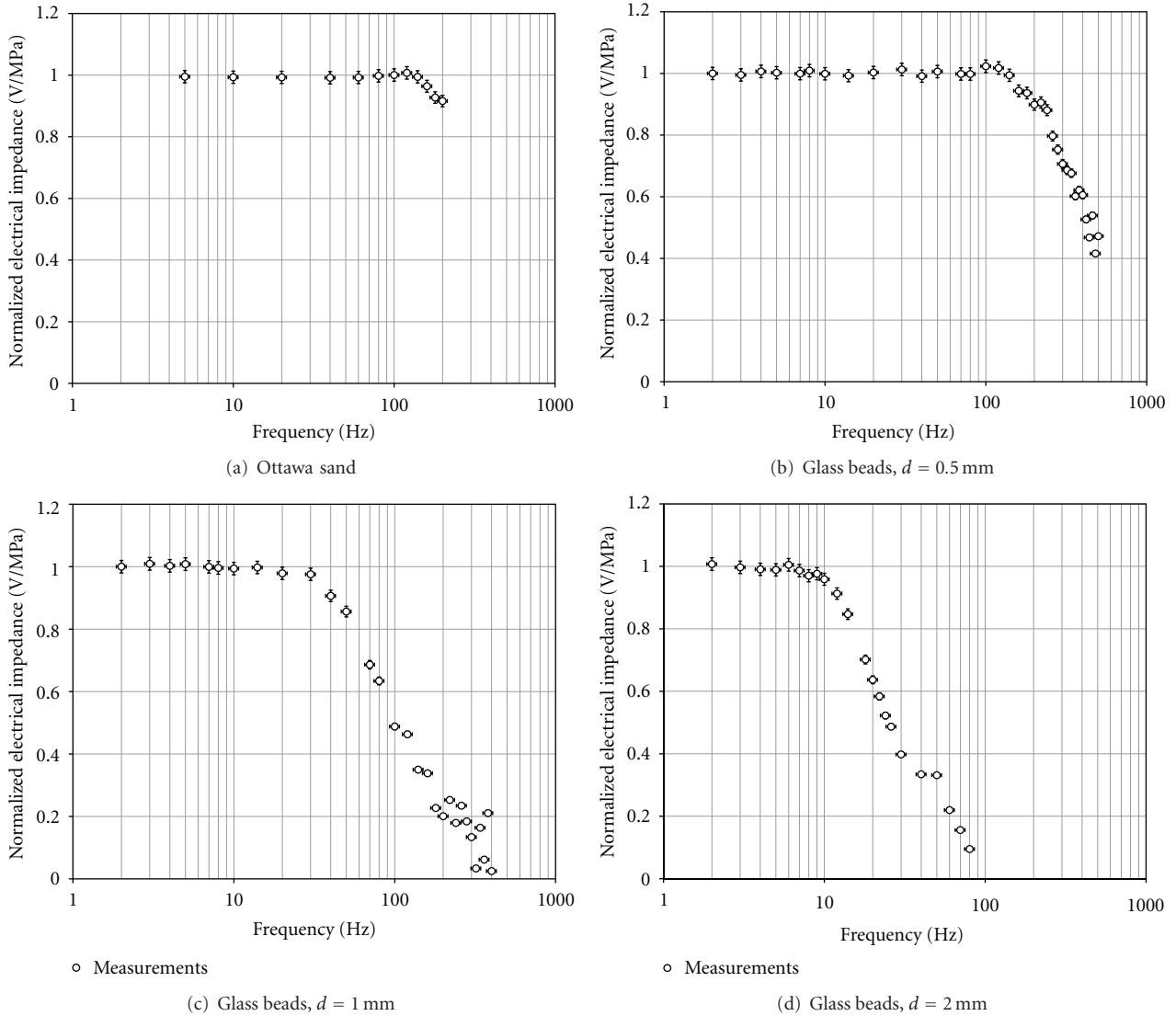
(d) Glass beads, $d = 2$ mm

FIGURE 2: Normalised electrical impedance data for (a) Ottawa sand, and glass beads with (b) $d = 0.5$ mm, (c) $d = 1$ mm, and (d) $d = 2$ mm.

differential fluid pressures at high frequencies, lowering the signal-to-noise ratio. One solution to this problem is to vary the drive current in order to generate a differential fluid pressure that can be measured with good signal-to-noise ratio and to keep that differential pressure constant for as great a range of frequencies as possible. Such a procedure implies that the piston amplitude will be different for each frequency. Current understanding of frequency-dependent streaming potentials does not indicate that there is a piston amplitude below which the coupling is not fully developed or any other reason why the streaming potential coupling coefficient should vary with piston amplitude. However, it is important experimentally to know if we will introduce any systematic errors by allowing the piston amplitude to vary and also to know if there is a piston amplitude below which measurements become unreliable due to the signal-to-noise ratio.

We have carried out tests to examine the measured streaming potential as a function of the piston amplitude using a sample of the Ottawa sand and an arbitrary frequency of 10 Hz. Dynamic fluid pressure, dynamic streaming potential, and instantaneous piston position measurements were made while decreasing the shaker driving current in increments (and hence the piston amplitude) until the measured values were below the noise threshold. Measurements were then made while incrementally increasing the driving current until the maximum displacement was reached.

The results are shown in Figure 1(b). The initial peak-to-peak displacement was just over 20 mm, and this decreased incrementally until it was 0.5 mm, then increased again to a maximum about 21.7 mm. In the range about 2 mm to 21.7 mm, the measured streaming potential and the calculated streaming potential coupling coefficient remained stable with $C_s = 0.5374 \pm 0.0029$ V/MPa, which represents a
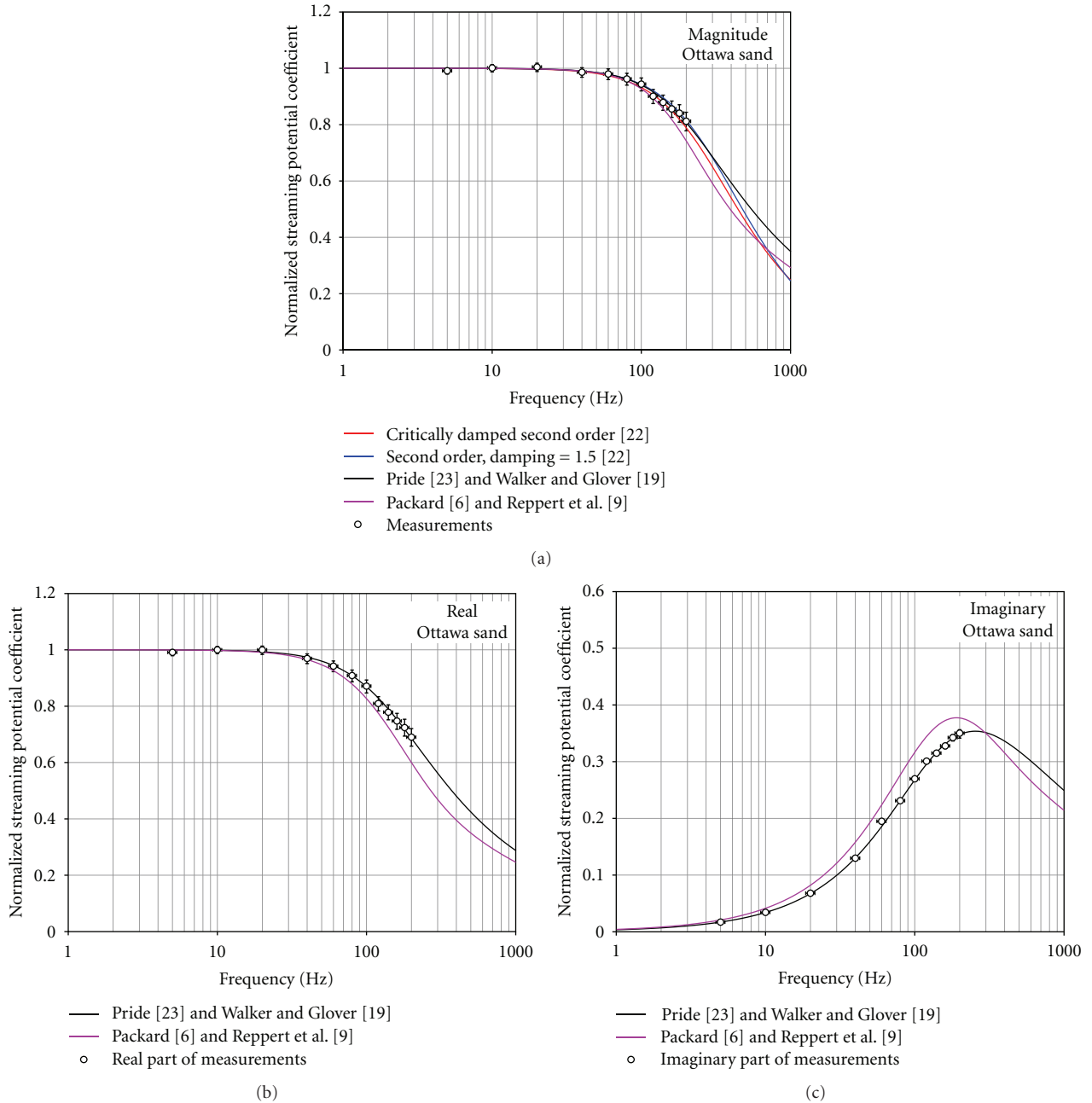
(a)

(b)

(c)

FIGURE 3: The calculated streaming potential coupling coefficient (normalised to the value at 5 Hz, which was 0.518 V/MPa) as a function of frequency for Ottawa sand saturated with 10^{-3} mol/L NaCl solution at 24°C ($\phi = 0.325$, $\kappa_{10} = 1.19 \times 10^{-10}$ m^2). (a) Magnitude with six models shown fitting the data [6, 9, 19, 22, 23], (b) real component for models [6, 9, 19, 23], and (c) imaginary component for models [6, 9, 19, 23].

variability of about 0.5%. The values during reduction and augmentation of piston displacement were $C_s = 0.5369 \pm 0.0026$ V/MPa and 0.5379 ± 0.0032 V/MPa, respectively, so there is no sensitivity to whether the piston amplitude is increasing or decreasing. We can remark, therefore, that in the range 2 mm to 21.7 mm the streaming potential and the calculated streaming potential coupling coefficient measured by this instrument are independent of piston amplitude and direction of piston amplitude change. Hence the piston

amplitude may be varied to optimize the measurement conditions.

The measured streaming potential was affected at piston amplitude less than about 2 mm. Under these conditions the measured pressure difference is very small for our high permeability sample, and it is difficult to distinguish the measurements from the background noise. We believe that the observed increase in the streaming potential coupling coefficient for displacements less than 2 mm is due to the
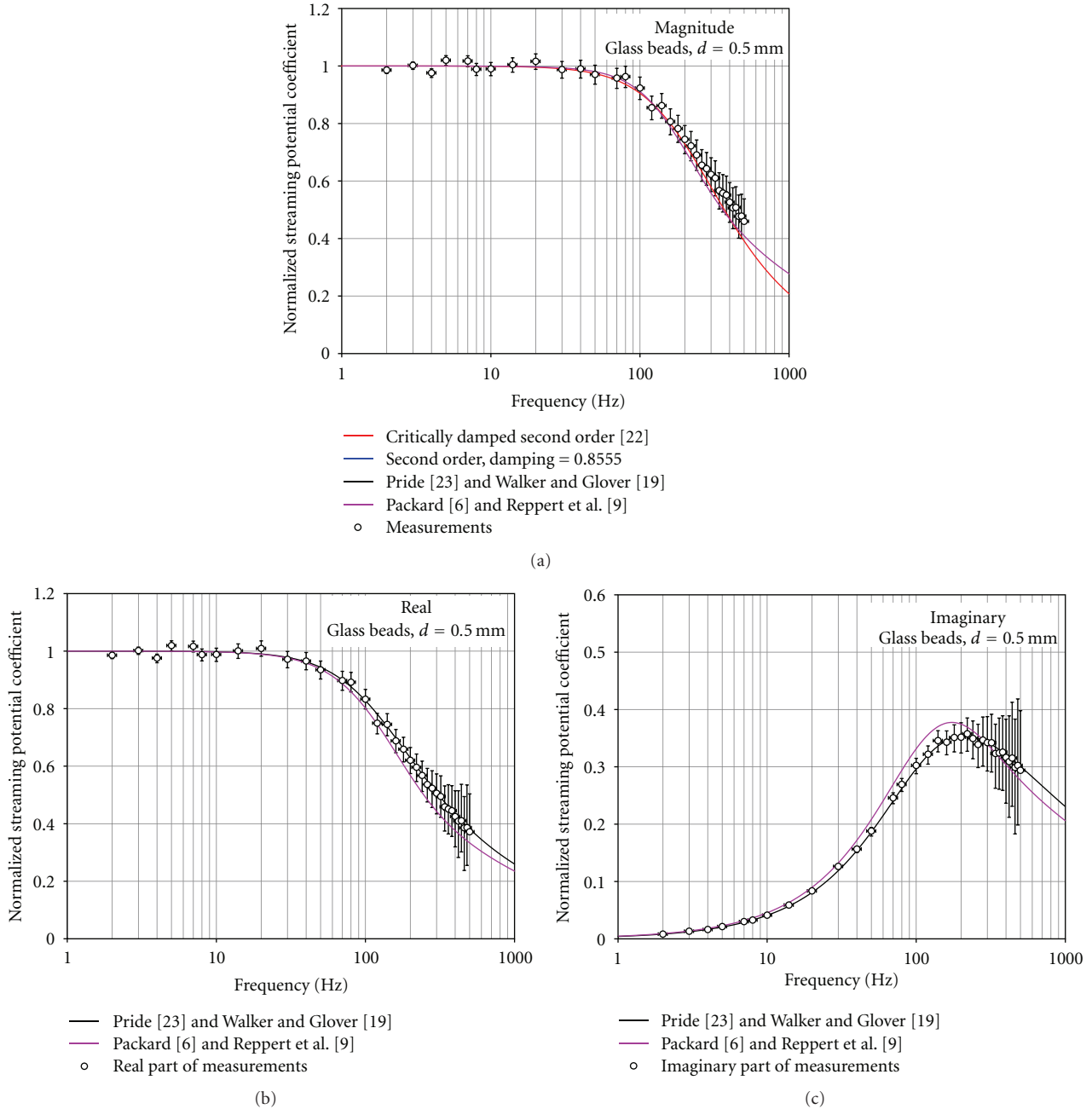
Figure 4: The calculated streaming potential coupling coefficient (normalised to the value at 2 Hz, which was 1.37 V/MPa) as a function of frequency for a pack of nominally 0.5 mm diameter glass beads saturated with 10^{-3} mol/L NaCl solution at 24°C ($\phi = 0.383$, $\kappa_{DC} = 1.62 \times 10^{-10}$ m²). (a) Magnitude with six models shown fitting the data [6, 9, 19, 22, 23], (b) real component for models [6, 9, 19, 23], and (c) imaginary component for models [6, 9, 19, 23].

difficulty in measuring these small pressures. There was no evidence for turbulent fluid flow at large piston amplitudes.

3.4. Initial Frequency-Dependent Streaming Potential Coupling Coefficient Results.
Figures 3, 4, 5 and 6 show the normalised measured streaming potential coupling coefficient for Ottawa sand and the three grades of glass bead as a function of frequency. The normalised streaming potential coup-

ling coefficient was calculated by dividing the measured streaming potential coupling coefficient at a given frequency by that measured at the lowest frequency available (5 Hz for Ottawa sand and 2 Hz for the glass beads). If one can assume that the streaming potential coupling coefficient at this low frequency approximates to that during steady-state flow, it is possible to say that the data shown in Figures 3–6 represent the right-hand side of (2), (3), (4), (11) and (14), that is, the frequency-dependent terms.
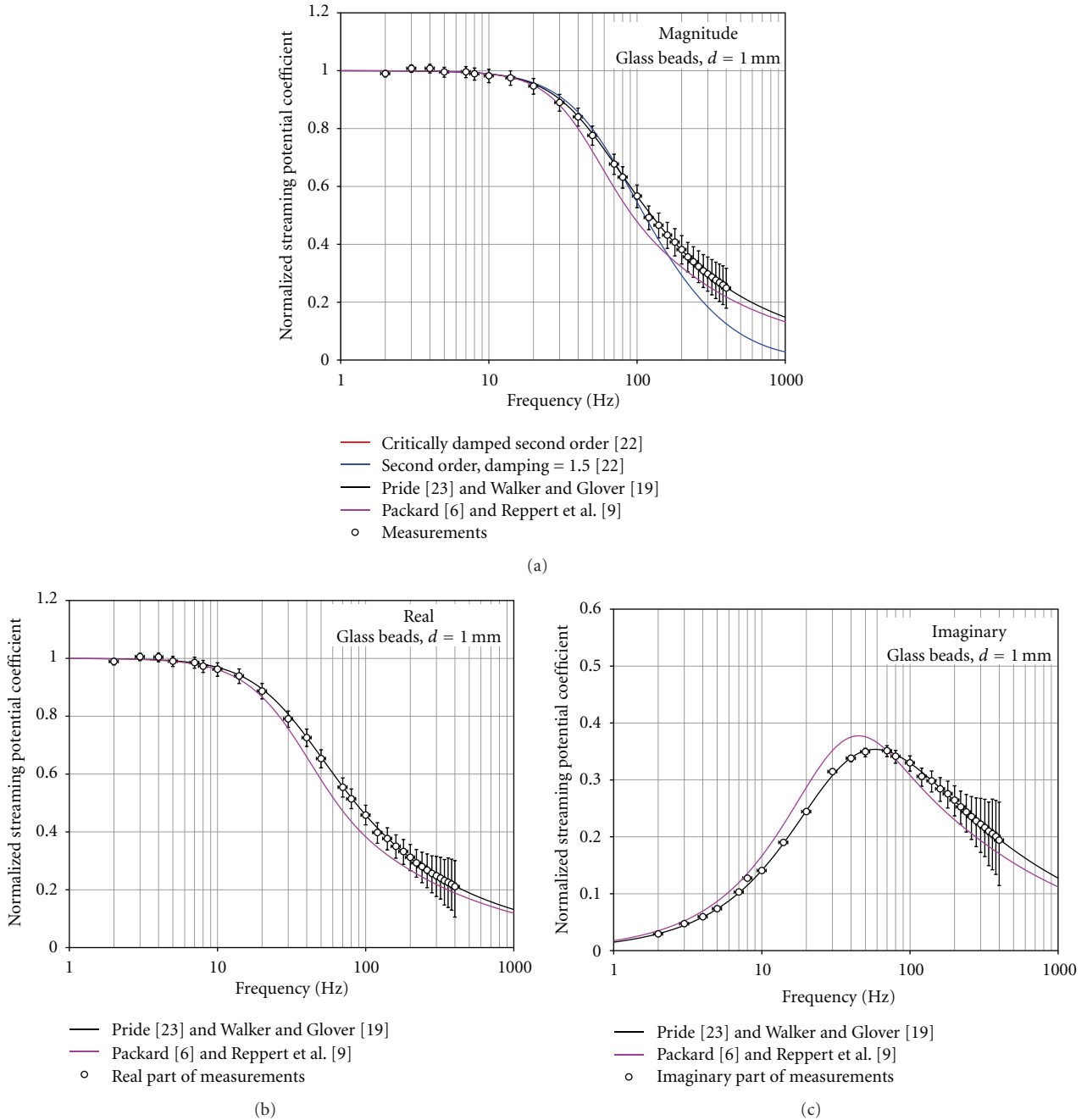
(a)

(b)

(c)

FIGURE 5: The calculated streaming potential coupling coefficient (normalised to the value at 2 Hz, which was 1.61 V/MPa) as a function of frequency for a pack of nominally 1 mm diameter glass beads saturated with 10^{-3} mol/L NaCl solution at 24°C ($\phi = 0.38$, $\kappa_{DC} = 5.95 \times 10^{-10}$ m^2). (a) Magnitude with six models shown fitting the data [6, 9, 19, 22, 23], (b) real component for models [6, 9, 19, 23], and (c) imaginary component for models [6, 9, 19, 23].

It should be noted in these figures that the error bars become larger at the higher frequencies. This is due to the difficulty in measuring small streaming potentials at frequencies greater than the transition frequency.

4. Analysis and Modelling of the Experimental Results

4.1. Steady-State Streaming Potential Coupling Coefficient. The majority of the data analysis will concentrate on the fre-

quency-dependent part of the streaming potential coupling coefficient. However, we should say a few words about the steady state streaming potential coupling coefficient. Although this was not measured in our apparatus, we can perhaps use the streaming potential coupling coefficient at the lowest frequency as a reasonable indication of that under true steady-state conditions considering that Figures 3–6 show that these values tend towards the steadystate value. The lowest frequency for the Ottawa sand was 5 Hz while those for the glass beads was 2 Hz. We will call the
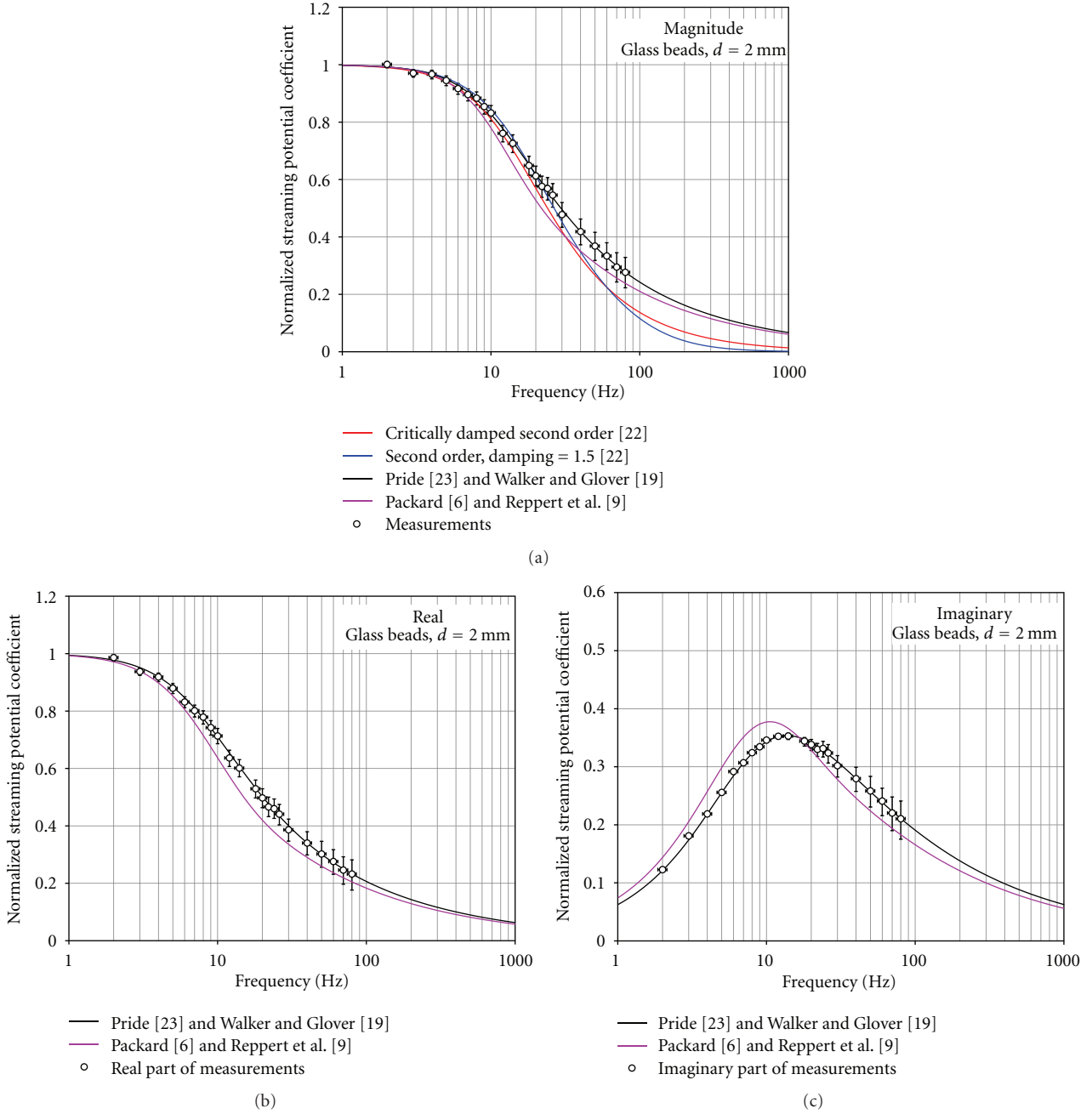
(a)

(b)

(c)

FIGURE 6: The calculated streaming potential coupling coefficient (normalised to the value at 2 Hz, which was 1.80 V/MPa) as a function of frequency for a pack of nominally 2 mm diameter glass beads saturated with 10^{-3} mol/L NaCl solution at 24°C ($\phi = 0.382$, $\kappa_{DC} = 27.2 \times 10^{-10}$ m^2). (a) Magnitude with six models shown fitting the data [6, 9, 19, 22, 23], (b) real component for models [6, 9, 19, 23], and (c) imaginary component for models [6, 9, 19, 23].

streaming potential coupling coefficients at these frequencies the quasi-steady-state values. The quasi-steady-state values of the streaming potential coupling coefficient for each of the samples are shown in Table 2. This table also shows some electrokinetic modelling that we have carried out using the same approach as Glover and Déry [17] and Glover et al. [16]. In this modelling we kept the following parameters constant: $\Gamma_o = 5$ sites/nm^2, pK$_{me} = 7.5$, pK$_- = 8$, while the formation factor, porosity, cementation exponent, grain

diameter fluid concentration, and pH were set to the values related to each sample (Table 1). It can be seen from Table 2 that the modelled values of the steady-state streaming potential coupling coefficient slightly overestimate the measured values. We need to put the measured and modelled values in the context of the measurements made by others and the experimental errors. Figure 7 shows the measured values and the model curves in the context of a database of other steady-state streaming potential coupling coefficient measurements

(a)

- ◆ database by Jaafar [31-32]
- ◇ Jaafar [31-32]
- —— Model Ottawa sand, pH 6
- —— Model glass beads, d = 0.5 mm, pH 6.4
- —— Model glass beads, d = 1 mm, pH 6.6
- —— Model glass beads, d = 2 mm, pH 6.7
- ▲ Measurement, Ottawa sand, pH 6
- ▲ Measurement, glass beads, d = 0.5 mm, pH 6.4
- ▲ Measurement, glass beads, d = 1 mm, pH 6.6
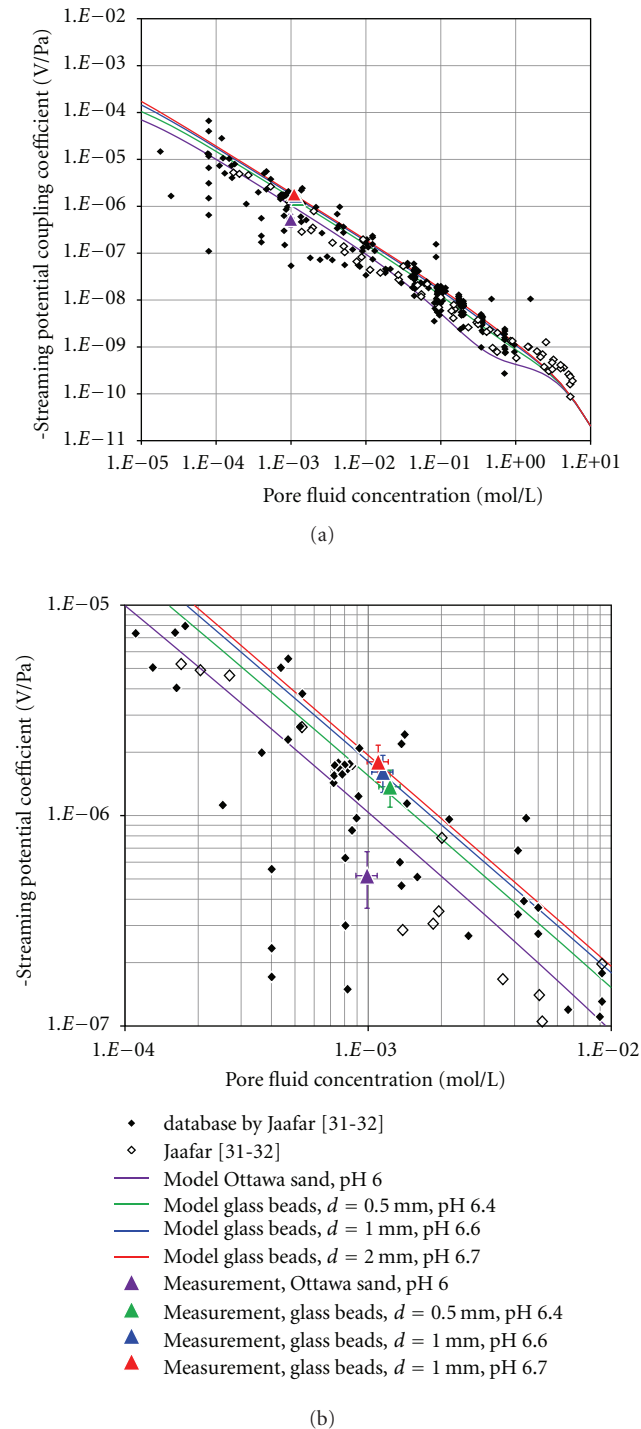- ▲ Measurement, glass beads, d = 1 mm, pH 6.7

(b)

FIGURE 7: (a) The steady-state streaming potential coupling coefficient measured in this work shown with a compilation of silica-based earth materials measured by (open symbols) or compiled by (solid symbols) Jaafar [31, 32]. The lines represent the theoretically modelled streaming potential coupling coefficient using the method of Glover et al. [16] and Glover and Déry [17] and with the parameters Γ_o = 5 sites/nm^2, pK$_{me}$ = 7.5, pK$_-$ = 8, and T = 24.0°C, with the porosity, cementation exponent, grain size, and pH for the individual samples (given in Table 1). (b) The same diagram as (a) on an expanded scale.

(from [31, 32]). It should be noted that the experimental values are plotted here at the fluid concentrations calculated from the fluid electrical conductivity that was measured on the fluid leaving the apparatus during the experiment rather than that of the original stock fluid, which was 0.001 mol/L. The error bars are approximate and represent a conservative assessment of the measurement errors (30% for the streaming potential coupling coefficient and 10% for the pore fluid concentration). It can be seen that the measured values are in fact in extremely good agreement with the existing data and the model. The model is extremely sensitive to the values of fluid concentration and pH used, and hence it is extremely important to have an accurate measurement of the pH value and the electrical conductivity of the fluid that emerges from the experimental apparatus during the experiment in order that the measurements can be compared with the model at an acceptable level of precision.

4.2. Frequency-Dependent Streaming Potential Coupling Coefficient. Figures 3–6 show the experimental data together with theoretical curves that (i) are based on standard equations in vibration mechanics, for example, [22], (ii) have been developed for capillary tubes [6, 9], and (iii) have been derived for porous media [19, 23]. In each figure there are three parts. The first shows the behaviour of the magnitude (absolute value, modulus) of the complex variable, while the other two parts show the real and imaginary components of the complex variable. The vibrational mechanics models [22], the Pride model [23], and its simplification [19] may all be fitted to the data to obtain the transition frequency ω_t, from which the characteristic pore radius of the sand can be calculated using (13), while the Packard model [6] and its simplification [9] may be used to obtain the effective capillary radius of the sand directly. A single curve is included for the Packard capillary tube model [6] and the Reppert et al. simplification [9] because they are indistinguishable at the scale of the figures and which indicates that the corrected Reppert et al. simplification (i.e., (8)) performs extremely well. The Pride model [23] and its simplification by Walker and Glover [19] are also represented by a single curve for the same reason.

Figures 3–6 show that all of the models describe the data fairly well. However, the following discussion shows that some of these fits do not use parameters that are consistent with other physical properties of the samples. The best fit for all the samples is provided by the Pride model [23] and its Walker and Glover simplification [19]. These models are specifically designed for porous media but do not implicitly take into account the surface conduction that occurs naturally in geological porous media. In fitting this model, we used the independently measured quasi-steady-state permeability k_{DC}, the electrical tortuosity τ_e that was calculated from the electrical impedance measurements, and the porosity by helium pycnometry ϕ, all of which are given in Table 1. The fitting variables were the transition frequency and the characteristic length scale of the pore space Λ. The values of the fitting variables are given in Table 2. The transition frequency can be used to derive an effective

Table 2: Summary of results.

Property	Unit	Ottawa sand	Glass beads			Comment
			0.5 mm	1 mm	2 mm	
Steady-state electrokinetic modelling						
Measured steady-state streaming potential coupling coefficient, C_{so}	V/MPa	0.518 ± 0.155	1.37 ± 0.411	1.61 ± 0.483	1.80 ± 0.54	Value at lowest frequency measured.
Modelled steady-state streaming potential coupling coefficient, C_{so}	V/MPa	1.05	1.26	1.57	1.76	Using [16, 17].
Modelled zeta potential, ζ	mV	−15.9	−29.6	−29.6	−29.6	Using [16, 17].
pH for electrokinetic modelling	—	6	6.7	6.7	6.7	
Transition frequencies						
Transition frequency, critically damped 2nd order vibrational model, ω_t	Hz	230	234	54	13	Using [22].
Transition frequency, 2nd order model with variable damping, ω_t	Hz	748.8	636.9	176.4	41.7	Using [22].
Damping factor, ξ	—	1.5	1.5	1.5	1.5	Using [22].
Transition frequency from the Pride model, ω_t	Hz	256.58	213	58.79	13.85	Using [23].
Transition frequency from the Glover and Walker simplification, ω_t	Hz	256.58	213.36	57.32	12.61	Using [19].
Predicted effective pore radius						
Calculated effective pore radius from independent measurement, r_p	μm	67.6 ± 16.2	70.8 ± 0.70	139 ± 3.41	287 ± 4.03	From Table 1
From the Packard model, equivalent capillary tube radius, r_{eff}	μm	67.5	72	145	302	Using [6].
From the critically damped 2nd order vibrational model	μm	70.46	69.85	145.41	296.35	Using (12)
From the Pride model	μm	66.71	73.21	139.36	287.11	Using (12)
From the Glover and Walker simplification	μm	66.71	73.15	141.13	300.90	Using (12)
Characteristic length scale, Λ	μm	62.40	67.76	131.45	280.24	Using (10)
Predicted permeabilities						
Measured permeability, κ_{meas}	m^2	1.19×10^{-10}	1.62×10^{-10}	5.95×10^{-10}	27.2×10^{-10}	See text.
Predicted permeability using the RGPZ method, κ_{RGPZ}	m^2	1.22×10^{-10}	1.52×10^{-10}	5.80×10^{-10}	24.8×10^{-10}	Using [26].
From the critically damped 2nd order vibrational model	m^2	1.33×10^{-10}	1.48×10^{-10}	6.32×10^{-10}	26.4×10^{-10}	Using (12)
From the Pride model	m^2	1.19×10^{-10}	1.62×10^{-10}	5.80×10^{-10}	24.8×10^{-10}	Using (12)
From the Glover and Walker simplification	m^2	1.19×10^{-10}	1.62×10^{-10}	5.95×10^{-10}	27.2×10^{-10}	Using (12)

pore size for the sample r_{eff} using (13), which is also given in Table 2. When this is done, it is clear that both Λ and r_{eff} agree well with the independently obtained pore size of the sample r_p (Tables 1 and 2). We conclude that the Pride model and its simplification perform extremely well when compared to experimental data.

While not as effective as the Pride model and its simplification, the Packard model [6] and its Reppert et al. simplification [9] also provide a fairly good fit to the data. However, the discrepancies between these models and the data clearly show that a model which is based on a bundle of capillary tubes is not as effective as the Pride model in describing a porous medium when the fluid flow and electrical flow have a tortuosity which is significantly different from unity such as in our samples where the electrical tortuosity is approximately 1.5 (see Table 1). Many rocks have tortuosities much higher than this. Hence, one would expect the Packard model and Reppert et al. models to perform worse for these rocks, overestimating the effective capillary radius and hence the predicted permeability of the sample. The advantage with these models is that when used with a single pore fluid at a constant temperature and pressure, they use a single variable: the effective capillary radius, which is shown in Table 2 for comparison with the independently measured value r_p.

The critically damped second-order vibrational mechanics model also provides a reasonable fit to the data, giving transition frequencies and effective pore radii that are consistent with the independently obtained measurements (Table 2). However, the variably damped second-order vibrational mechanics model has difficulty fitting the data. Here there are two fitting parameters, the transition frequency and the damping coefficient. A large number of different combinations of these parameters provide curves that seem to fit the experimental data approximately. Figures 3–6 show one particular combination where the damping coefficient $\xi = 1.5$ and the transition frequencies are given in Table 2. The transition frequencies are clearly much too large and predict effective pore radii that are badly underestimated. Increasing the damping coefficient further allows the frequency roll-off to approach the experimental data, but only at the expense of even higher predicted transition frequencies. We conclude, therefore, that this model is of no practical use when describing frequency-dependent streaming potential coefficients of porous media.

4.3. Sensitivity of the Pride Model to Steady-State Permeability.
The full Pride model calculates the transition frequency from the sample porosity, electrical tortuosity, and permeability as well as the density and viscosity of the pore fluid (9). It also calculates a parameter which we have called m^* (10) from the porosity, characteristic length scale of the pores Λ, the electrical tortuosity, and the permeability of the sample. It became clear in our modelling that the fit to the experimental data depends strongly on the value of m^*, which in turn depends upon the steady-state permeability of the rock k_{DC}, its electrical tortuosity τ_e, and its porosity ϕ as well as the characteristic length scale of its pores Λ. While τ_e, ϕ, and Λ vary from sample to sample, they can
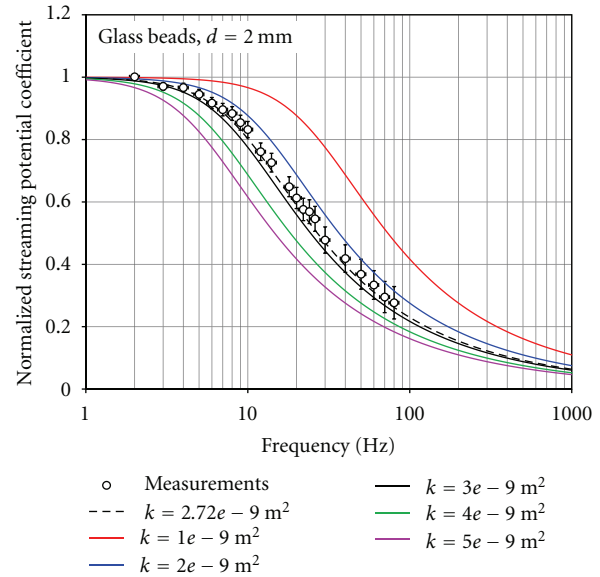

Figure 8: The calculated streaming potential coupling coefficient (normalised to the value at 2 Hz, which was 1.80 V/MPa) as a function of frequency using the Pride model [23] for a pack of nominally 2 mm diameter glass beads saturated with 10^{-3} mol/L NaCl solution at 24°C ($\phi = 0.382$, $\kappa_{\text{DC}} = 27.2 \times 10^{-10}$ m^2). Each solid curve shows the results of the model for a different value of permeability. The dashed line is for the permeability of the sample that was measured independently.

be measured independently. This is also true of the steady-state permeability of the rock. However, the steady-state permeability of the rock can vary over many orders of magnitude which makes the Pride model extremely sensitive to this parameter. Figure 8 shows the Pride model for a range of different permeabilities from 1×10^{-9} m^2 to 5×10^{-9} m^2 and the other parameters matching those for our 2 mm glass bead dataset. It is worthwhile noting that this is a very small permeability range considering (i) the precision that is usual when measuring permeability in the laboratory and (ii) the natural variability of permeability from sample to sample even in isotropic, homogeneous clean reservoir rocks. While this sensitivity might be considered to be a problem when forward modelling, it is a huge advantage when backward modelling as it should allow the predicted permeability to have a very high precision. Hence, although these measurements are currently difficult to make, they have the potential of providing an extremely precise method of obtaining the permeability of porous media.

4.4. Transition Frequencies and Pore Sizes.
The transition frequencies and capillary radii calculated from each of the 5 models are given in Table 2. All of the transition frequencies, except those from the second order vibrational mechanics model with variable damping, are in broad agreement and vary according to the pore size of the sample. Figure 9 shows all the existing data as compiled by Tardif et al. [11] together with the Ottawa sand data of [11] and the new glass bead data presented in this paper. The dashed lines represent the
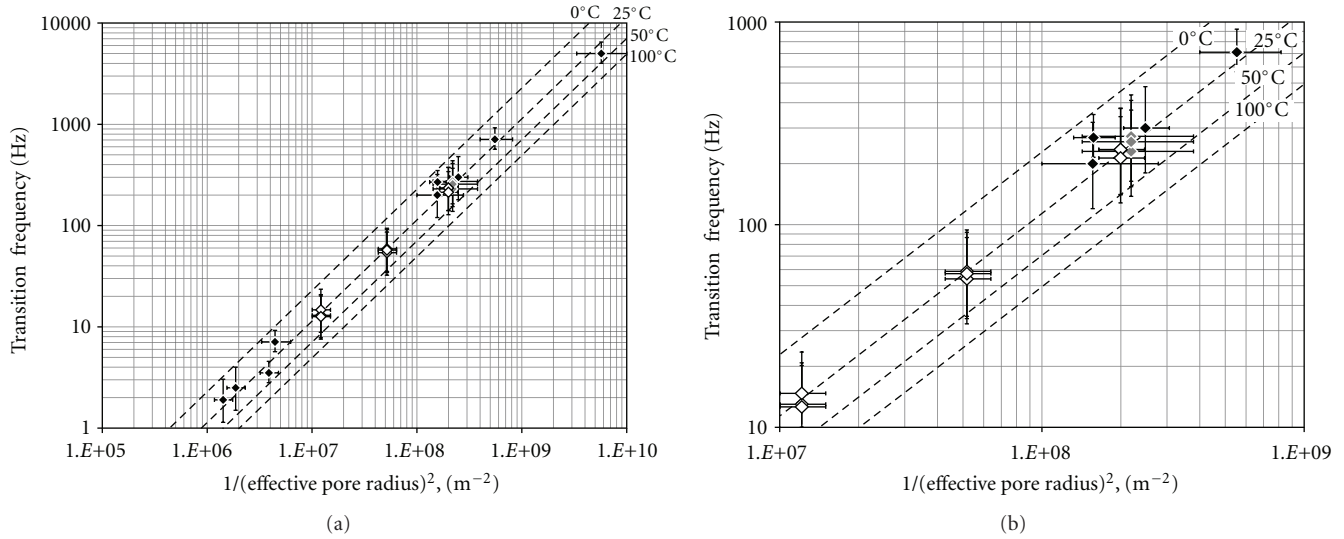
(a)

(b)

Figure 9: The electrokinetic transition frequency as a function of the inverse square characteristic pore size (a) in full and (b) at expanded scale. Black symbols, previous data for capillary tubes, filters frits, and rocks, Figure 6 of [19]; grey symbols, Ottawa sand measured at $24.0°C \pm 0.8°C$; open symbols, glass bead packs. The dashed lines represent the theoretical result [19] at four different temperatures.

result of (13) [19] using the fluid viscosities and densities for the pore fluid at various different temperatures. It is clear that the new data are compatible with the independently obtained effective pore radius measurements.

The transition frequency can be used to predict the effective pore radius of each sample using (13). Table 2 shows that all the predictions are in good agreement with the value of effective pore radius derived from the measured grain diameter using the method of Glover and Walker [12] and with the equivalent capillary radius derived from the Packard model [6].

The transition frequency can be used to predict the steady-state permeability of the sample using (13). Table 2 shows that all the predictions are in good agreement with the measured values of permeability and the permeability predicted using the RGPZ method [26]. It should be noted that the predictions for the porous media models [19, 23] are exact because the permeability is an input to these models. Hence, these models can only be used to predict permeability if they are fitted to the experimental data with the permeability as a variable parameter.

5. Conclusions

We have used the electromagnetic drive approach to create an experimental apparatus to measure the dynamic streaming potential coupling coefficient of disaggregated porous media between 1 Hz and 1 kHz. The apparatus has been used to measure samples of Ottawa sand and glass bead packs. Measurements were made on Ottawa sand between 5 Hz and 200 Hz, and on glass bead packs between 2 Hz and 500 Hz. In most cases the full variation either side of the transition frequency was captured. Measurements were possible up to

1 kHz, but in practice the streaming potential values became so small at high frequencies that they were unreliable; only those with reasonably small errors have been included in this paper.

Analysis of the steady-state part of the measured data, shows that the measured steady-state streaming potential coupling coefficient is compatible with the latest theoretical models of electrokinetics.

The dynamic experimental data, in the form of normalised streaming potential coupling coefficient, have been fitted with five theoretical models that were derived (i) from vibrational mechanics theory, (ii) for bundles of capillary tubes, and (iii) for porous media. The Pride model and its simplification, which were developed for porous media, fitted the data best and provided transition frequencies, characteristic length scales, and effective pore radii that were consistent with independently measured values for the samples. The Packard model and its simplification, which were developed for capillary tubes, also performed well. The second order vibrational mechanics model with variable damping only fitted the data when unreasonable transition frequencies were used, but the critically damped second order vibrational model performed reasonably well.

We found that the Pride model and its simplification models are extremely sensitive to the steady-state permeability which may cause difficulties in forward modelling given that this parameter is rarely known precisely and that there is often a large range of permeabilities even in isotropic, homogeneous, clean reservoir rock. However, the sensitivity is an advantage in reverse modelling as it should allow precise permeability determinations to be made by fitting this model to experimental dynamic streaming potential coupling coefficient data.

Acknowledgments

References

[1] P. W. J. Glover, J. Ruel, and E. Tardif, "Frequency-dependent streaming potential of porous media: 1. Experimental approaches and apparatus design," *International Journal of Geophysics*. In press.

[2] C. Bordes, L. Jouniaux, S. Garambois, M. Dietrich, J. P. Pozzi, and S. Gaffet, "Evidence of the theoretically predicted seismomagnetic conversion," *Geophysical Journal International*, vol. 174, no. 2, pp. 489–504, 2008.

[3] C. Bordes, L. Jouniaux, M. Dietrich, J. P. Pozzi, and S. Garambois, "First laboratory measurements of seismo-magnetic conversions in fluid-filled Fontainebleau sand," *Geophysical Research Letters*, vol. 33, no. 1, Article ID L01302, 2006.

[4] R. Chandler, "Transient streaming potential measurements on fluid-saturated porous structures: an experimental verification of biot's slow wave in the quasi-static limit," *Journal of the Acoustical Society of America*, vol. 70, no. 1, pp. 116–121, 1981.

[5] P. M. Reppert and F. D. Morgan, "Streaming potential collection and data processing techniques," *Journal of Colloid and Interface Science*, vol. 233, no. 2, pp. 348–355, 2001.

[6] R. G. Packard, "Streaming potentials across glass capillaries for sinusoidal pressure," *The Journal of Chemical Physics*, vol. 21, no. 2, pp. 303–307, 1953.

[7] C. E. Cooke, "Study of electrokinetic effects using sinusoidal pressure and voltage," *The Journal of Chemical Physics*, vol. 23, no. 12, pp. 2299–2303, 1955.

[8] A. R. Sears and J. N. Groves, "The use of oscillating laminar flow streaming potential measurements to determine the zeta potential of a capillary surface," *Journal of Colloid and Interface Science*, vol. 65, no. 3, pp. 479–482, 1978.

[9] P. M. Reppert, F. D. Morgan, D. P. Lesmes, and L. Jouniaux, "Frequency-dependent streaming potentials," *Journal of Colloid and Interface Science*, vol. 234, no. 1, pp. 194–203, 2001.

[10] P. M. Reppert, *Electrokinetics in the earth*, Ph.D. thesis, Massachusetts Institute of Technology, 2000.

[11] E. Tardif, P. W.J. Glover, and J. Ruel, "Frequency-dependent streaming potential of Ottawa sand," *Journal of Geophysical Research B*, vol. 116, no. 4, Article ID B04206, 2011.

[12] P. W. J. Glover and E. Walker, "A grain-size to effective pore-size transformation derived from electrokinetic theory," *Geophysics*, vol. 74, no. 1, pp. E17–E29, 2009.

[13] F. D. Morgan, E. R. Williams, and T. R. Madden, "Streaming potential properties of Westerly granite with applications," *Journal of Geophysical Research B*, vol. 94, no. 9, pp. 12449–12461, 1989.

[14] P. M. Reppert and F. D. Morgan, "Temperature-dependent streaming potentials: 1. Theory," *Journal of Geophysical Research B*, vol. 108, no. 11, pp. 3–12, 2003.

[15] P. M. Reppert and F. D. Morgan, "Temperature-dependent streaming potentials: 2. Laboratory," *Journal of Geophysical Research B*, vol. 108, no. 11, pp. 4–13, 2003.

[16] P. W. J. Glover, E. Walker, and M. D. Jackson, "Streaming-potential coefficient of reservoir rock: A theoretical model," *Geophysics*, vol. 77, no. 2, pp. D17–D43, 2012.

[17] P. W. J. Glover and N. Déry, "Streaming potential coupling coefficient of quartz glass bead packs: dependence on grain diameter, pore size, and pore throat radius," *Geophysics*, vol. 75, no. 6, pp. F225–F241, 2010.

[18] D. L. Johnson, J. Koplik, and R. Dashen, "Theory of dynamic permeability and tortuosity in fluid-saturated porous media," *Journal of Fluid Mechanics*, vol. 176, pp. 379–402, 1987.

[19] E. Walker and P. W. J. Glover, "Characteristic pore size, permeability and the electrokinetic coupling coefficient transition frequency in porous media," *Geophysics*, vol. 75, no. 6, pp. E235–E246, 2010.

[20] A. Revil and L. M. Cathles III, "Permeability of shaly sands," *Water Resources Research*, vol. 35, no. 3, pp. 651–662, 1999.

[21] A. Revil, P. A. Pezard, and P. W. J. Glover, "Streaming potential in porous media 1. Theory of the zeta potential," *Journal of Geophysical Research B*, vol. 104, no. 9, pp. 20021–20031, 1999.

[22] W. T. Thomson and M. D. Dahleh, *Theory of Vibration with Applications*, Prentice Hall, 1998.

[23] S. Pride, "Governing equations for the coupled electromagnetics and acoustics of porous media," *Physical Review B*, vol. 50, no. 21, pp. 15678–15696, 1994.

[24] E. Charlaix, A. P. Kushnick, and J. P. Stokes, "Experimental study of dynamic permeability in porous media," *Physical Review Letters*, vol. 61, no. 14, pp. 1595–1598, 1988.

[25] P. W. J. Glover and E. Walker, "Modelling the frequency dependence of hydraulic flow and streaming potential coupling coefficients in capillary bundles and porous rocks," in *Proceedings of the Annual Congress of European Geosciences Union*, paper A-02892, Vienna, Austria7, April 2008.

[26] P. W. J. Glover, I. I. Zadjali, and K. A. Frew, "Permeability prediction from MICP and NMR data using an electrokinetic approach," *Geophysics*, vol. 71, no. 4, pp. F49–F60, 2006.

[27] S. N. Lvov and R. H. Wood, "Equation of state of aqueous NaCl solutions over a wide range of temperatures, pressures and concentrations," *Fluid Phase Equilibria*, vol. 60, no. 3, pp. 273–287, 1990.

[28] S.L. Phillips, H. Ozbek, and R.J. Otto, "Basic energy properties of electrolytic solutions database," in *Proceedings of the 6th International CODATA Conference*, Santa Flavia, Italy, May 1978, http://www.osti.gov/bridge/purl.cover.jsp;jsessionid =3954E775156A8BC0FA35DB5CE5B402D4? purl=/ 6269880-iPJPhB/ DB5CE5B402D4?purl =/6269880-iPJPhB/.

[29] P. N. Sen and P. A. Goode, "Influence of temperature on electrical conductivity on shaly sands," *Geophysics*, vol. 57, no. 1, pp. 89–96, 1992.

[30] P. Leroy, A. Revil, A. Kemna, P. Cosenza, and A. Ghorbani, "Complex conductivity of water-saturated packs of glass beads," *Journal of Colloid and Interface Science*, vol. 321, no. 1, pp. 103–117, 2008.

[31] M. Z. Jaafar, J. Vinogradov, and M. D. Jackson, "Measurement of streaming potential coupling coefficient in sandstones saturated with high salinity NaCl brine," *Geophysical Research Letters*, vol. 36, no. 21, Article ID L21306, 2009.

[32] J. Vinogradov, M. Z. Jaafar, and M. D. Jackson, "Measurement of streaming potential coupling coefficient in sandstones saturated with natural and artificial brines at high salinity," *Journal of Geophysical Research B*, vol. 115, no. 12, Article ID B12204, 2010.

[33] P. W. J. Glover, "What is the cementation exponent? A new interpretation," *The Leading Edge*, vol. 28, no. 1, pp. 82–85, 2009.

[34] P. W. J. Glover, "A generalized Archie's law for n phases," *Geophysics*, vol. 75, no. 6, pp. E247–E265, 2010.